

Enhance Charge Transfer and Reduce Internal Resistance for Triboelectric Nanogenerator via Switching Charge Shuttling

Xin Guo, Yuqi Wang, Yuming Feng, Yang Yu, Jianlong Wang, Siyang He, Jinzhi Zhu, Hengyu Li, Tinghai Cheng,* Zhong Lin Wang,* and Xiaojun Cheng*

Traditional triboelectric nanogenerators (TENGs) face significant challenges related to low charge density and high internal impedance. Many methods have been proposed to enhance the surface charge density of TENGs, yet they do not simultaneously achieve low internal resistance. Here, a switch-shuttling triboelectric nanogenerator (SS-TENG) is proposed. By periodically interrupting the circuit during the intrinsic capacitance variation of the TENG during the charge shuttle process, the SS-TENG alters the potential difference while maintaining a constant charge in the capacitor, thereby enhancing energy storage and improving overall output performance. The rapid activation of the switch significantly reduces internal resistance. Compared to traditional charge shuttle TENGs, the charge transfer amount increases by 1.9 times, while the short-circuit current rises by 9.6 times, with internal resistance reduced by a factor of 20. Furthermore, a prototype of the novel cylindrical-hexagram bluff body (CHB) vortex-induced vibration energy harvester based on the SS-TENG is designed and tested, demonstrating its ability to reliably harvest energy from underwater tidal flows and surface wave energy. Additionally, a self-powered marine pollution detection strategy has been developed using the SS-TENG. This work provides valuable insights for enhancing the performance of TENGs and actively promotes their commercialization.

sustainable, mobile, and distributed energy sources has significantly increased.^[1-3] In this context, the mechanical energy associated with human activities presents an ideal power source for energy harvesting. Among the various energy harvesting technologies, triboelectric nanogenerators (TENGs) have garnered substantial attention due to their lightweight design, cost-effectiveness, wide selection of materials, and efficiency in harvesting low-frequency energy.^[4-8] Since their invention by Zhong Lin Wang's group in 2012,^[9] TENGs have demonstrated significant potential in diverse applications, including self-powered sensors,^[10-14] micro/nano power sources,^[15-20] and blue energy harvesting.^[21-24] TENGs, as a promising energy harvesting technology, require enhanced output performance to expand their application potential.^[20-28]

To enhance the performance of TENGs, a range of strategies has been implemented, including ion injection, material selection, surface modification, optimization of the contact process,

triboelectrification enhancement effect, and external charge boosting.^[29-35] Techniques such as ion injection are widely used to increase surface charge density.^[36] Surface modification of materials can enhance the generation of contact charges, with a focus on ensuring that the processing does not compromise the mechanical strength of the materials.^[37,38] Optimization of the contact process facilitates the coupling of contact, sliding, and separation motions, demonstrating excellent output performance and significant durability. However, the complexity of the contact process increases the design difficulty of prototypes.^[34] The triboelectrification enhancement effect is a straightforward and universal method that can significantly improve the output performance of TENGs, albeit at the expense of additional pre-processing for the friction materials.^[35] Recently, charge pumping methods have addressed the limitations of traditional tribo-materials in contact electrification and are widely used to enhance charge density.^[39-42] These methods greatly enhance the electrical output performance of the TENGs and broaden their range of applications. However, TENGs still face the challenge of high impedance, which leads to significant impedance mismatch when directly interfaced with storage devices such as

1. Introduction

With the rapid advancement of passive environmental monitoring sensors and the Internet of Things (IoT), the demand for

X. Guo, Y. Wang, Y. Feng, Y. Yu, J. Wang, S. He, J. Zhu, H. Li, T. Cheng, Z. L. Wang, X. Cheng
Beijing Institute of Nanoenergy and Nanosystems
Chinese Academy of Sciences
Beijing 101400, P. R. China
E-mail: chengtinghai@binn.cas.cn; zhong.wang@mse.gatech.edu; chengxiaojun@binn.cas.cn

X. Guo, Y. Wang, Y. Feng, Y. Yu, J. Wang, S. He, H. Li, T. Cheng, X. Cheng
School of Nanoscience and Engineering
University of Chinese Academy of Sciences
Beijing 100049, P. R. China
T. Cheng, Z. L. Wang, X. Cheng
Guangzhou Institute of Blue Energy
Guangzhou 510555, P. R. China

 The ORCID identification number(s) for the author(s) of this article can be found under <https://doi.org/10.1002/aenm.202405116>

DOI: 10.1002/aenm.202405116

batteries or capacitors, thereby diminishing energy conversion efficiency.^[43,44] Therefore, further improvements in charge transfer and reductions in internal resistance are essential for advancing the commercialization of TENGs.

In this work, a switch-shuttling triboelectric nanogenerator (SS-TENG) is proposed, aimed at addressing the limitations of conventional TENGs in energy harvesting efficiency and environmental adaptability. The SS-TENG employs a periodic switching mechanism that allows for an increase in the potential difference between its electrodes while maintaining a constant charge within the TENG, thereby enhancing the power output during the charge transfer process. Through a combination of theoretical analysis and experimental validation, we demonstrate this design results in a remarkable increase in performance, with experimental results showing a 1.9-fold increase in charge transfer and a 9.6-fold enhancement in short-circuit current compared to traditional charge-shuttle TENGs. Furthermore, internal resistance is dramatically reduced from 200 to just 10 MΩ, resulting in more efficient power utilization. A prototype of the novel cylindrical hexagram bluff body (CHB) vortex-induced vibration energy harvester is also introduced, stabilizing energy collection from tidal and wave energy, making the system well-suited for nearshore regions rich in tidal currents. This research further explores the integration of the SS-TENG with seawater quality monitoring systems, utilizing its dual energy harvesting capabilities to support marine environmental monitoring through the detection of ocean temperature changes and dissolved solids. This study provides a strategy for achieving high power output and reducing internal resistance, thereby enhancing the future application potential of TENGs.

2. Results and Discussion

The magnitude of transferred charge (Q_{SC}), short-circuit current (I_{SC}), and internal resistance of the triboelectric nanogenerators (TENGs) are the key parameters for evaluating their performance. In this work, the optimization of these objectives achieved simultaneously by switching shuttles is shown in **Figure 1a**. The basic concept of the device is shown in **Figure 1b**. The SS-TENG consists mainly of a pump TENG, a main TENG, a buffer capacitor, and a synchronous switch. Functioning as a power source, the pump TENG injects oppositely charged particles into the two electrodes of the buffer capacitor through a rectifier bridge. The buffer capacitor is a ceramic capacitor, and its capacitance remains constant. A conductive loop is formed between the main TENG and the buffer capacitor through two wires, with a synchronous switch installed on one of the wires. The switch moves synchronously with the main TENG, closing when the two electrodes of the main TENG make contact and when they reach their maximum separation, and remaining open during all other phases. During the contact-separation process of the main TENG, its changing capacitance generates a voltage difference with the buffer capacitor. Due to the presence of the switch, this voltage difference is amplified, leading to an increase in the symmetrical transfer of charges between the main TENG and the buffer capacitor. The operating principle of the SS-TENG can be understood by examining the charge and discharge behavior of a parallel plate capacitor. The capacitance of a parallel plate capacitor is influenced by factors such as the separation between

the plates, the area of overlap, and the type of dielectric material placed between them.

As shown in **Figure 1c-i**, when the capacitor is linked to a power source, the two plates carry equal amounts of charge with opposite signs. As illustrated in **Figure 1c-ii**, when the separation between the plates increases, the capacitance decreases, reducing the amount of charge the capacitor can hold and thus decreasing the stored energy. Conversely, reducing the plate distance causes the reverse process, which is straightforward to understand. To store more energy in the capacitor, the amount of charge should remain constant. As shown in **Figure 1c-iii**, when the capacitor is fully charged at maximum capacitance and then disconnected from the power source, increasing the plate distance decreases the capacitance while keeping the charge on the plate constant. This leads to a significant increase in the stored energy and the potential difference across the plates. When connected to a load, the capacitor can release energy more quickly and in larger amounts. Using Equations (1) and (2), it is possible to calculate the changes in potential and energy of the capacitor after the switch is turned off, assuming the charge on the capacitor remains unchanged while the separation between the plates of the parallel-plate capacitor is modified.

$$Q = V \times C \quad (1)$$

$$W = \frac{Q \times V}{2} = \frac{Q^2}{2C} \quad (2)$$

where W refers to the energy accumulated in the capacitor, and Q signifies the charge held by the capacitor. Thus, the factors contributing to the performance enhancement of the SS-TENG can be clarified based on the previously discussed principles. Similarly, the main TENG can be viewed as a parallel plate capacitor with a varying plate separation, as illustrated in **Figure 1d-i**. In the first stage, when the plates are closest together, and the capacitance is at its peak, the voltage drops below that of the buffer capacitor, leading to charge transfer from the buffer capacitor to the main TENG. In the second stage (**Figure 1d-ii**), as the separation between the plates grows, the synchronous switch is activated. In the third stage (**Figure 1d-iii**), when the plate distance reaches its maximum, the switch closes, enabling charge transfer from the main TENG to the buffer capacitor, resulting in power output to the load. With the application of external force again, the gap between the dielectric films steadily decreases, eventually becoming zero when complete contact is achieved (**Figure 1d-i**). This concludes a complete energy transfer cycle. Throughout the working cycle, the SS-TENG prevents charge leakage in the outer circuit, allowing for the establishment of a maximum potential difference between the electrodes and boosting the TENG's power output. The charge stored in the buffer capacitor during each cycle, output by the main TENG, is calculated using Equation (3).^[45]

$$Q_c = \frac{C \Delta V}{t f} \quad (3)$$

where C represents the capacity of the buffer capacitor, ΔV denotes the stored voltage, t refers to the operational time, and f indicates the contact frequency of the synchronous switch. Due to its inherent capacitive characteristics, the TENG exhibits high impedance. When coupled with low-impedance energy storage

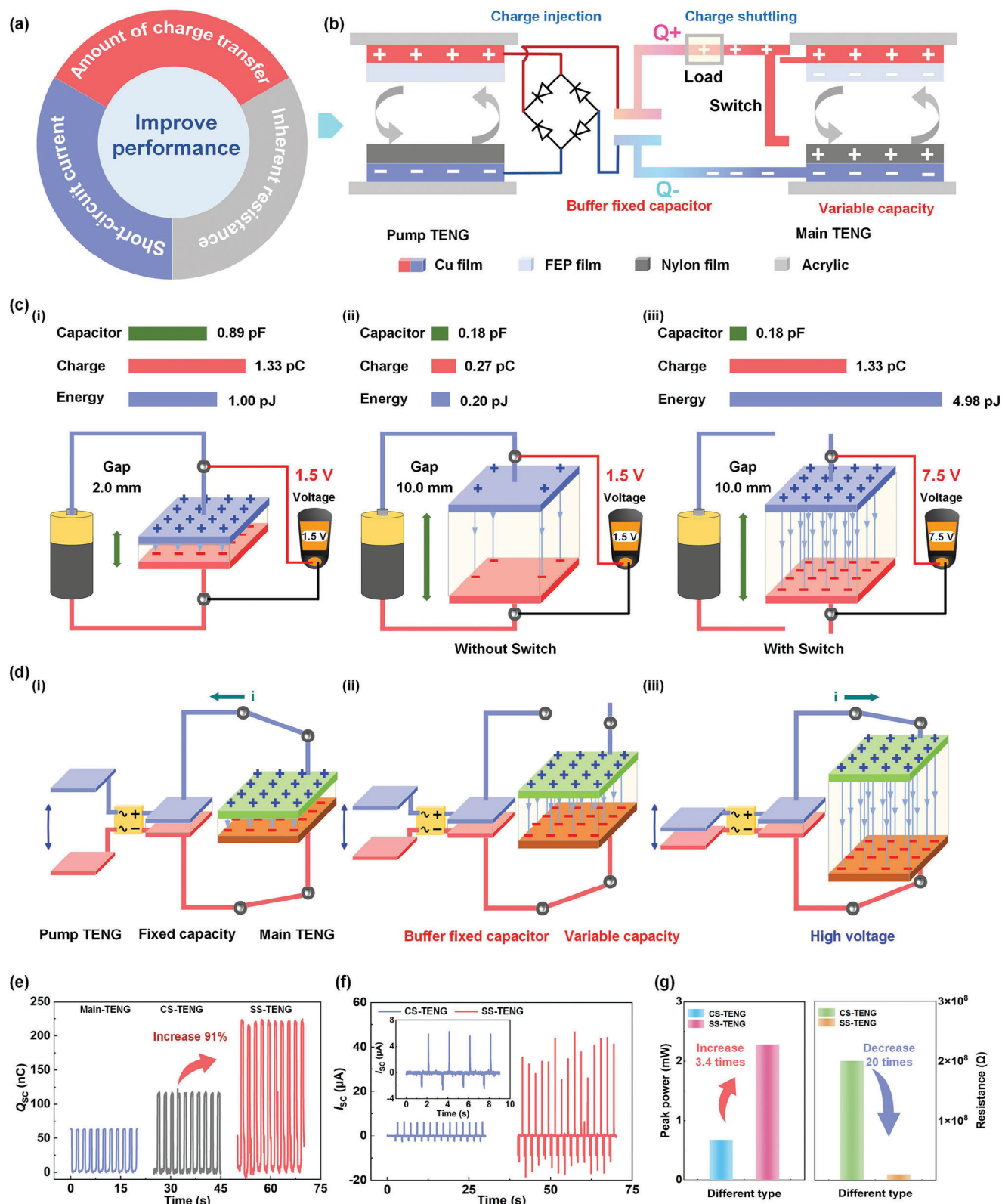


Figure 1. Mechanism and electrical performance of SS-TENG a) Power generation performance of SS-TENG increases. b) Schematic diagram of charge shuttle model of synchronous switch. c) Function of switch in charging capacity process. d) Charge transfer process and power generation enhancement principle. e) Effect of increasing transferred charge. f) Comparison of current in different modes. g) Effect of power improvement and internal resistance reduction.

units or devices, this significant impedance mismatch can result in low energy utilization efficiency. The optimal load resistance (R_0) for the TENG can be estimated using Equation (4),^[45] typically falling within the range of $M\Omega$.

$$R_0 \approx \frac{(\epsilon_e + d_{\max})^2}{S\nu\epsilon_0} \quad (4)$$

where ϵ_e signifies the effective dielectric constant, d_{\max} indicates the maximum distance between the electrodes of the main TENG, S represents the contact area, ν denotes the average velocity, and ϵ_0 the vacuum dielectric constant. From Equation (4), it can be seen that the internal resistance of the SS-TENG is influenced by its structural parameters and motion speed. The rapid closure of the synchronous switch at the moment of contact is a key factor in reducing the internal resistance of the SS-TENG.

To demonstrate the enhanced performance of the SS-TENG, a comparative analysis of its charge transfer capabilities was conducted against those of contact-separation mode TENG models and charge-shuttling triboelectric nanogenerators (CS-TENG). As depicted in Figure 1e, the charge transfer of the SS-TENG exceeds that of the charge-shuttling triboelectric nanogenerators by a factor of more than 1.9 and surpasses that of the contact-separation TENG by a factor of 3.7. Furthermore, as depicted in Movie S1 (Supporting Information), the transition from the traditional CS-TENG to the SS-TENG results in an immediate increase in charge transfer, achieving its maximum value within 5 cycles. Upon implementing a synchronous switch, the I_{SC} of the SS-TENG is enhanced by a factor of 9.6, as shown in Figure 1f. The internal resistance of the SS-TENG decreases from 200 to 10 $M\Omega$, representing a 20-fold decrease, while the peak power output is increased by a factor of 3.4 (Figure 1g).

Notably, the SS-TENG not only enhances output performance but also reduces internal resistance, making it more practical. This advancement is achieved without any treatment of the triboelectric materials or the need for additional circuit elements.

2.1. Electrical Properties of SS-TENG

To gain a deeper insight into the features of the SS-TENG, an experimental system was designed with asynchronous contact between the main TENG and the pump TENG, as depicted in Figure 2a. The stators of the main TENG and the pump TENG were equipped with a synchronous switch on the same plane, ensuring that the switch is triggered when the main TENG reaches both contact and maximum separation. Both the main TENG and the pump TENG utilize nylon film and fluorinated ethylene propylene (FEP) film as dielectric layers, each configured as squares with sides measuring 50 mm. The synchronous switch is made of conductive copper foil with an area of 1 cm^2 . Figure 2b shows the I_{SC} of the SS-TENG under identical conditions. The findings demonstrate a 9.6-fold increase in the I_{SC} of the SS-TENG compared to the charge shuttle mode TENG, reaching 43.6 μA . This current increase is primarily attributed to the reduced discharge time and the increase in transferred charge, as shown in Figure 2c. Figure 2d illustrates the charge transfer process under the same conditions, showing that the initial charge transfer of the SS-TENG is relatively slow but rapidly increases to

227.08 nC. Furthermore, the SS-TENG not only exhibits a significant increase in charge but also maintains a constant duty cycle, as shown in Figure 2e,f.

The charge output characteristics of the SS-TENG in two domains are illustrated in Figure 2g. The amount of charge transferred through the load is identical on both sides, with the switch and the side without the switch, allowing energy to be collected from both sides simultaneously. The output power of the SS-TENG is compared with that of the CS-TENG in Figure 2h. The output power of the SS-TENG is 2.28 mW, while that of the CS-TENG is 0.67 mW, and this comparison was made based on the significant reduction in the internal resistance of the SS-TENG. Additionally, Figure 2i illustrates the voltage-charge curves for both the SS-TENG and the CS-TENG. The energy per single wave for the SS-TENG is 44.52 μJ , which is 6.11 times greater than that of the CS-TENG (7.28 μJ).

Further investigation into the types of triboelectric materials, contact forces between electrodes, and contact-separation frequencies reveal their effects on the functionality of the SS-TENG. As illustrated in Figure 2j, an enhancement in the efficiency of the SS-TENG is observed both between polymer materials and between polymer and metal materials. Among the tested combinations, the nylon film and FEP film exhibit the highest output performance. Figure 2k illustrates that when the buffer capacitor is configured to 3.3 nF, a higher shuttle charge is achieved. As illustrated in Figure 2l and Figure S3 (Supporting Information), the effects of contact frequency and contact force on the SS-TENG exhibit a similar trend: as both the contact frequency and force increase, the transferred charge also increases, and the time required to reach charge saturation decreases.

2.2. Structure of the Integrated Device Based on the SS-TENG

Given the wide range of potential applications of the SS-TENG, it can serve as a fundamental component in environmental energy collection and autonomous monitoring systems. To evaluate the energy harvesting capabilities of SS-TENG under various external excitations, an energy harvesting device was fabricated using a spring oscillator system, as illustrated in Figure 3a. The pump TENG is positioned in the lower part of the SS-TENG, while the main TENG is located in the upper part, with the synchronous switch moving along with the actuator section of the SS-TENG, as presented in Figure 3b. The spring-damping system of the SS-TENG is depicted in Figure 3c. Since there is no spring positioned in the space separating the main TENG's electrode pair, the vibration model can be represented as a single-degree-of-freedom system for simplification purposes.

Building on the theoretical assessment and experimental findings discussed earlier, additional experiments were performed to explore how external excitation parameters affect the output performance of the SS-TENG. Initially, the SS-TENG was configured as a single-degree-of-freedom vibration system and driven vertically by a linear motor (Figure S4, Supporting Information). The results are presented in Figure 3d,e,f. Under constant displacement, the power generation of the SS-TENG improved as the acceleration rose from 1 to 5 m s^{-2} . The associated output curves

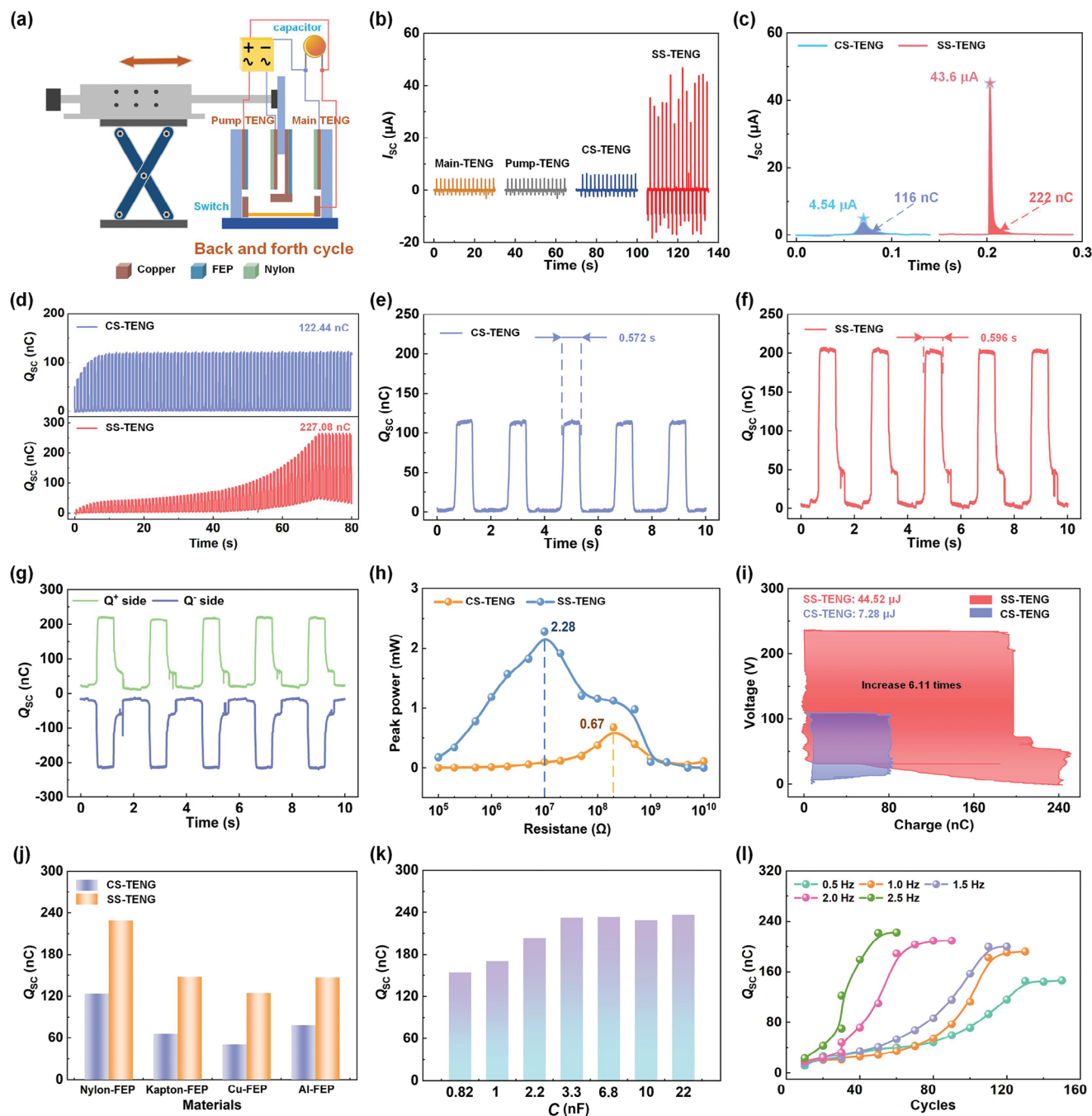


Figure 2. Output performance of SS-TENG and CS-TENG. a) Electrode motion simulation. b) Current comparison across different modes. c) Amplified view of individual current peaks. d) Transferred charge versus transfer time comparison. e) CS-TENG transfer charge waveform. f) SS-TENG transfer charge waveform. g) Comparison of transferred charge on both sides. h) Comparison of SS-TENG power with CS-TENG. i) The voltage-charge curve of SS-TENG and CS-TENG. j) Transferred charge comparison between SS-TENG and CS-TENG using various triboelectric material pairs. k) Comparison of charge with different buffer capacitors. l) Transferred charge of SS-TENG with various frequencies.

are illustrated in Figure S5 (Supporting Information). Furthermore, under constant acceleration, variations in displacement from 30 to 90 mm resulted in negligible changes in open-circuit voltage (V_{OC}), I_{SC} , and Q_{SC} . Notably, despite fluctuations in external excitation, the enhancement in output performance provided by the SS-TENG remained stable in relation to the CS-TENG.

The SS-TENG is capable of being fabricated into a multi-layer integrated structure, with a side-view schematic of the integrated device provided in Figure 3g. Through the use of a frame connection, multiple layers of SS-TENGs can achieve synchronous contact separation, with the switches closing simultaneously to ensure concurrent energy output. In the configuration depicted in

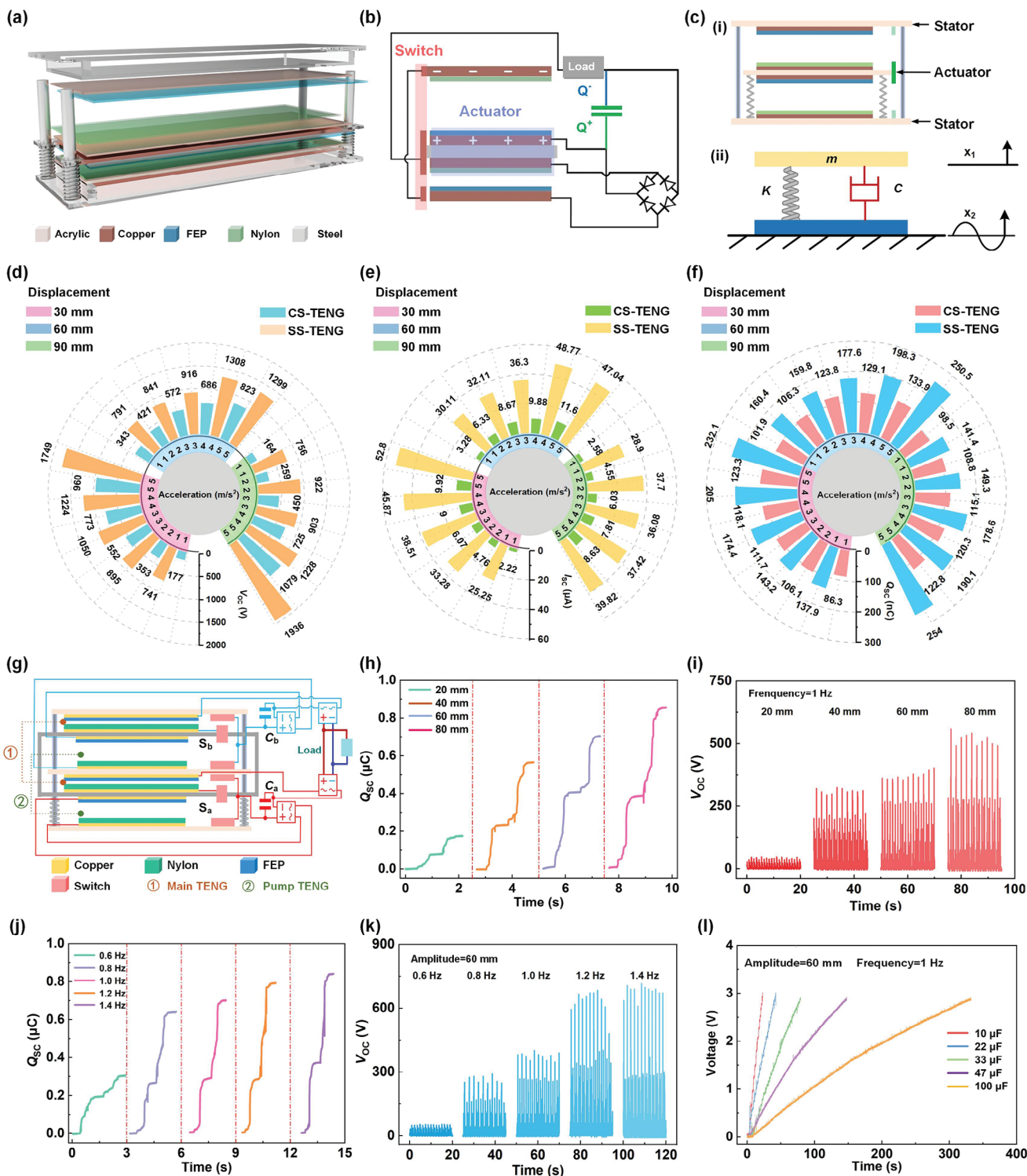


Figure 3. Performance of the integrated power generation unit. a) Schematic diagram of the power generation unit. b) Schematic of the upper and lower vibration synchronized switching pumping operation. c) Generator spring oscillator model. d) Voltage comparison at different displacements and accelerations. e) Comparison of current at different displacements and accelerations. f) Comparison of transferred charges at different displacements and accelerations. g) Circuit diagram of the integrated device. h) Comparison of individual cycle charges for different displacements after parallel rectification. i) Voltage comparison for different amplitudes. j) Comparison of single-cycle charge at different amplitudes after parallel rectification. k) Comparison of voltage at different frequencies. l) Charge capacity time.

Figure 3g, multiple SS-TENG units are integrated, with S_a and S_b representing the synchronous switches for different layers, and C_a and C_b as the corresponding buffer capacitors. With a driving rate of 1 Hz and a displacement of 80 mm, the integrated prototype achieved a charge transfer of 0.87 μC per cycle, with a V_{OC} of 555 V (Figure 3h,i). To further demonstrate the SS-TENG's ability to harvest energy at low frequencies, the system was driven at low frequencies ranging from 0.6 to 1.4 Hz. As illustrated in Figure 3j, the SS-TENG transferred 0.843 μC of charge per cycle at a driving rate of 1.4 Hz and a displacement of 60 mm, achieving a V_{OC} of 698 V (Figure 3k). At a driving frequency of 1 Hz, the device charges a 100 μF capacitor to 3 V in a span of 327 s, demonstrating its high efficiency in energy harvesting under these operating conditions (Figure 3l).

2.3. Dynamic Performance Optimization of SS-TENG

The gravitational forces exerted by the Moon and the Sun cause periodic fluctuations in the Earth's ocean surface, leading to two distinct movements: the vertical rise and fall of seawater due to tides and the horizontal movement caused by tidal currents.

To validate the environmental energy harvesting capability of the proposed method, this paper presents a prototype of tidal energy harvesting based on the SS-TENG, with its structure illustrated in Figure 4a. The prototype primarily consists of a bluff body, a spring, and a guide rail. The bluff body is designed with an internal cavity, housing the single-degree-of-freedom SS-TENG, which moves in sync with the bluff body. Since the SS-TENG is enclosed within the bluff body, the prototype is well-suited for efficiently harvesting underwater tidal current energy. A cylindrical acrylic protective shell surrounds the SS-TENG, shielding it from water leakage and protecting the electrodes, as shown in Figure S6 (Supporting Information). The prototype harnesses the vibrations induced by vortex shedding. As fluid flows around the bluff body, pressure vortices are generated, causing the bluff body to oscillate and enabling energy harvesting. Figure 4b illustrates the profile and pressure distribution contours of the bluff body. Due to the periodic pressure differences on the bluff body surface, the net force, F_a , acting on the bluff body results from the combined forces in the X and Y directions. The guide rail restricts movement in the X direction, leading to vertical oscillations of the bluff body (Figure 4c).

In this work, to better validate the energy harvesting capabilities of the SS-TENG in tidal current applications, a cylindrical hexagram bluff body (CHB) was proposed, characterized by six vertices protruding from a circular base, as illustrated in Figure 4d-i. Subsequently, the dynamic performance of the CHB is compared with various bluff body shapes, including square, trapezoidal, circular, and hexagonal cross-sections, under unidirectional water flow. Details regarding the mesh generation and boundary conditions utilized in the simulations are provided in Figure S7 (Supporting Information). Figure 4d presents the vorticity contours for each bluff body, with the results indicating that the CHB generates a wider initial vortex detachment, signifying stronger vortex shedding. A comparison of displacement in the Y-direction reveals that the CHB exhibits greater upward and downward displacement (Figure 4e). Similarly, the lift coefficient and torque follow the same trend as the displacement, as shown

in Figure 4f,g. This explains why the dynamic performance of the CHB outperforms the other bluff bodies. Figure S8 (Supporting Information) presents the pressure distribution contours for each bluff body, further demonstrating the suitability of the CHB for tidal current energy harvesting.

2.4. Performance of the Device for Tidal Current Energy Harvesting

Based on the statistical data in Table S1 (Supporting Information), it can be concluded that tidal current energy is predominantly concentrated in coastal regions. The primary energy distribution is characterized by unidirectional oscillatory flow below the water surface and surface waves above (Figure 5a). As depicted in Figure 5b, seawater is influenced by the ebb and flow of the tides, resulting in two distinct forms of motion: underwater movement driven by tidal currents and surface movement driven by waves. The prototype operates through vertical reciprocating motion in both scenarios, allowing it to harvest energy from both tidal flows and surface waves. To validate the energy harvesting capability of the above method in an aquatic environment, a simulated setup was constructed to evaluate its optimized performance under different conditions. As the flow velocity rises from 0.27 to 0.61 m s^{-1} , the prototype operates through vertical reciprocating motion in both scenarios, allowing it to harvest energy from both tidal flows and surface waves. Maintains a stable output, with the V_{OC} around 130 V, the I_{SC} approximately 39.6 μA , and the Q_{SC} around 248 nC, regardless of whether the flow is in the forward or reverse direction (Figure 5c,d,e). These results demonstrate that the prototype operates through vertical reciprocating motion in both scenarios, allowing it to harness energy from tidal flows as well as waves at the surface. Operates effectively at a water flow velocity of 0.27 m s^{-1} . Given the stability of the output, the prototype operates through vertical reciprocating motion in both scenarios, enabling it to harvest energy from tidal flows and surface waves across varying flow speeds and directions. At a flow velocity of 0.45 m s^{-1} , the peak power output reached 3.11 mW (Figure 5f). The consistent performance of the prototype can be further analyzed by evaluating the Q_{SC} and the frequency of the waveforms (Figure 5g). Within this range of flow velocities, vortex-induced vibrations exhibit a self-locking frequency mechanism, which ensures stable power output and mitigates significant fluctuations that could potentially damage electrical components.

When the prototype floats on the water surface, it can be driven by surface waves. A testing system was constructed to evaluate its energy harvesting performance under real wave conditions, as illustrated in Figure S9 (Supporting Information). This system simulates a wave environment using a linear motor, transmission mechanism, and oscillating plate. As shown in Figure 5h, the prototype can initiate operation with an oscillation frequency of 0.4 Hz and achieves a peak output when the wave frequency reaches 0.6 Hz, resulting in a V_{OC} of 173.2 V. Similar to the tidal current operation, the prototype can efficiently harvest energy from both forward-facing and reverse-facing waves, reaching a maximum I_{SC} at 51.3 μA while generating 276.0 nC in Q_{SC} , as shown in Figure 5i,j. This is attributed to the symmetric design of the CHB structure.

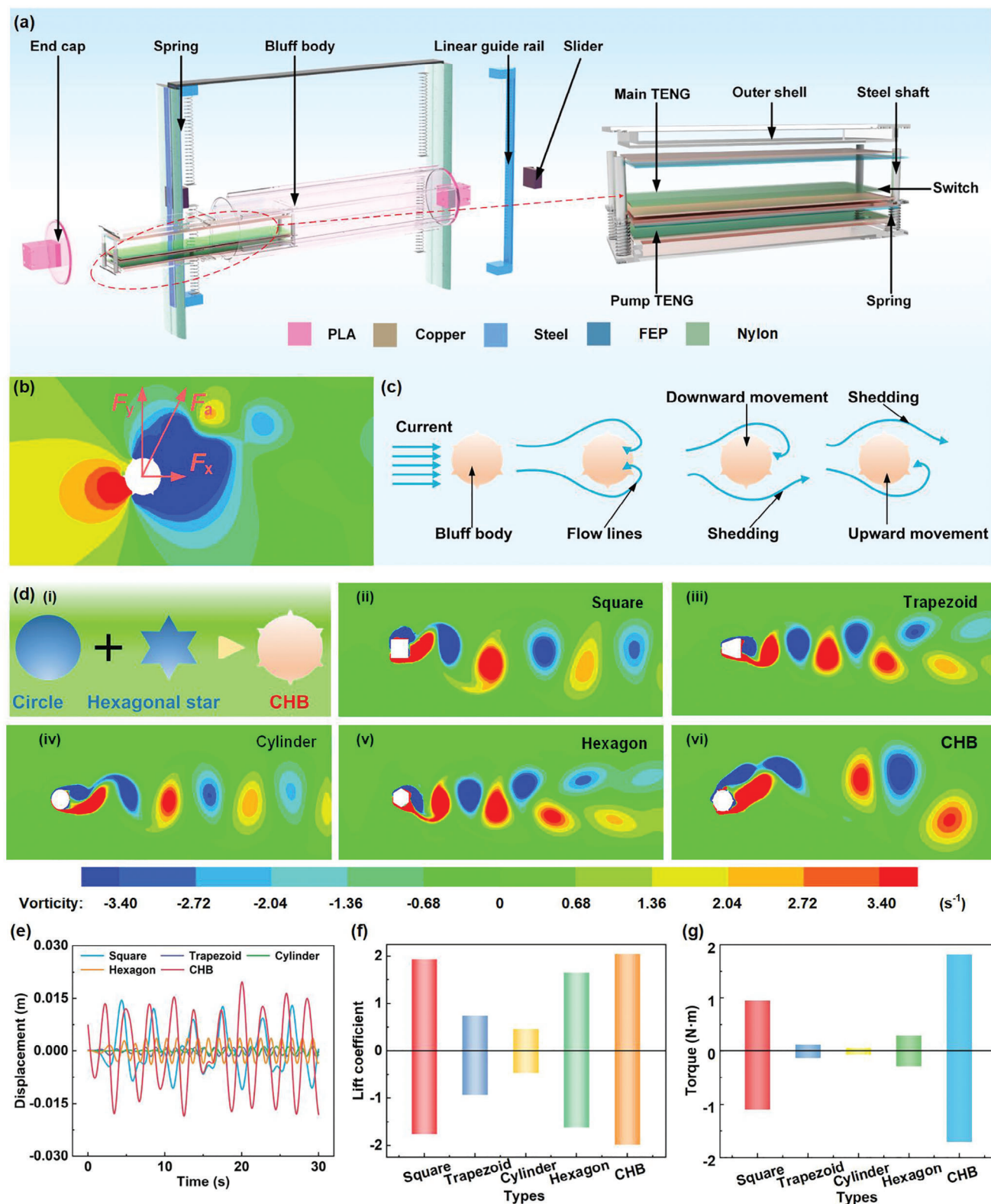


Figure 4. SS-TENG-based low-speed hydrodynamic energy harvesting system. a) Schematic of the structure of the flow-induced vibration generator. b) Schematic diagram of the force on the bluff body. c) Schematic diagram of the motion process. d) Shedding of vortices for different passivation in different states. e) Comparison of displacements of different obturators in the same condition. f) Comparison of lift coefficients for different blunt bodies. g) Comparison of torque for different blunt bodies.

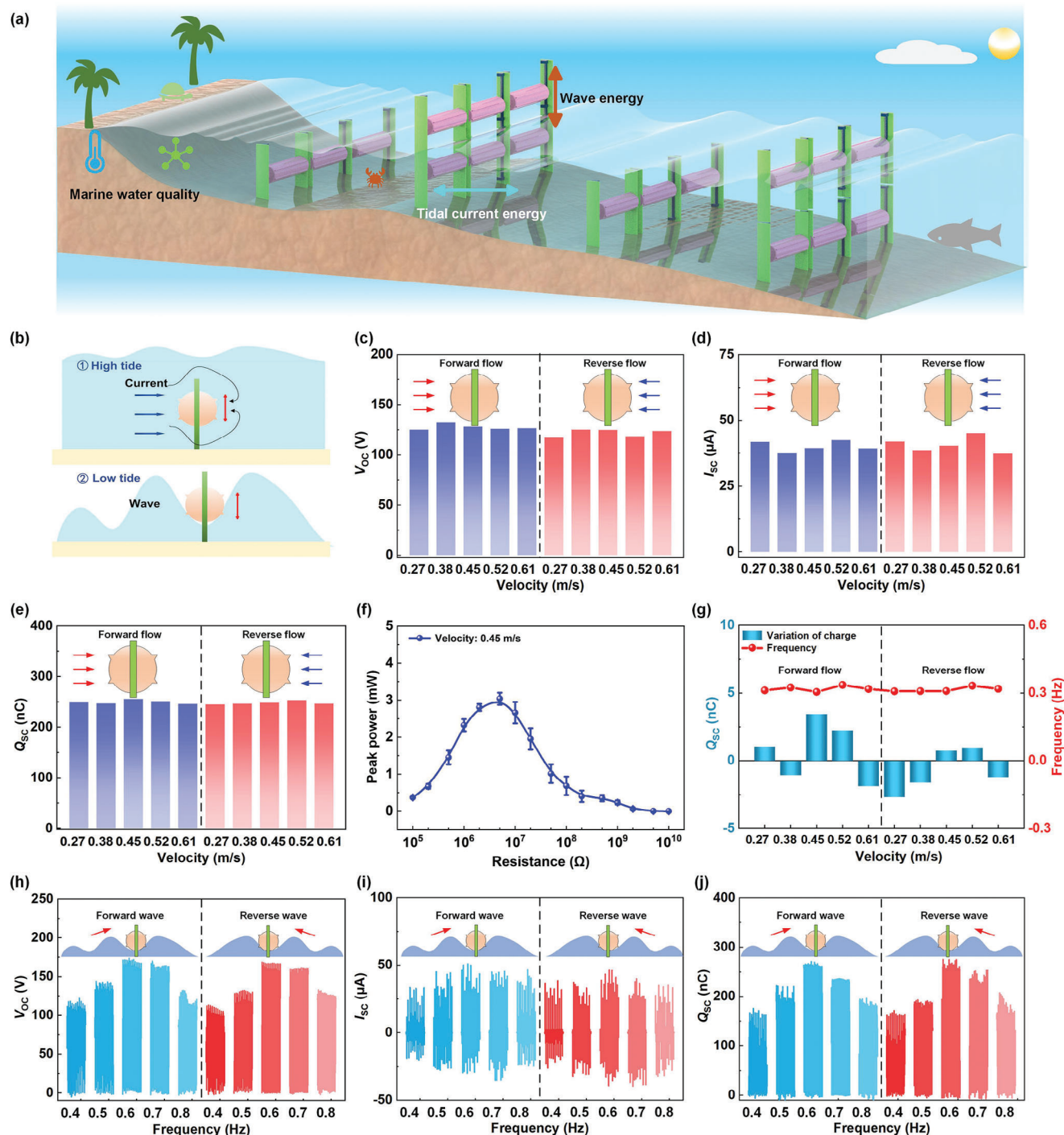


Figure 5. SS-TENG underwater performance. a) Schematic diagram of tidal current energy. b) SS-TENG kinematic mode type. c) Voltage for different flow velocities. d) Current for different flow velocities. e) Charge at different flow velocities. f) Power at different flow rates. g) Charge frequency fluctuation rates for different flow velocities. h) Voltage at different wave frequencies. i) Current at different wave frequencies. j) Charge at different wave frequencies.

2.5. Practical Applications and Demonstrations of the SS-TENG

Further improvement of the electrical efficiency of the SS-TENG was achieved by implementing a power management circuit (PMC) to accelerate the charging process. As illustrated in **Figure 6a**, the PMC consists of two parts: the pre-stage circuit

and the post-stage circuit. The working principle is as follows: the signal output from the SS-TENG is stored in the pre-stage capacitor (C_{in}) via inductor (L_1). Together, L_1 and C_{in} form an LC oscillation circuit that amplifies the pre-stage output signal. When the voltage across C_{in} reaches the threshold voltage of the PMOS transistor, switch S_2 closes, allowing energy to be stored in output

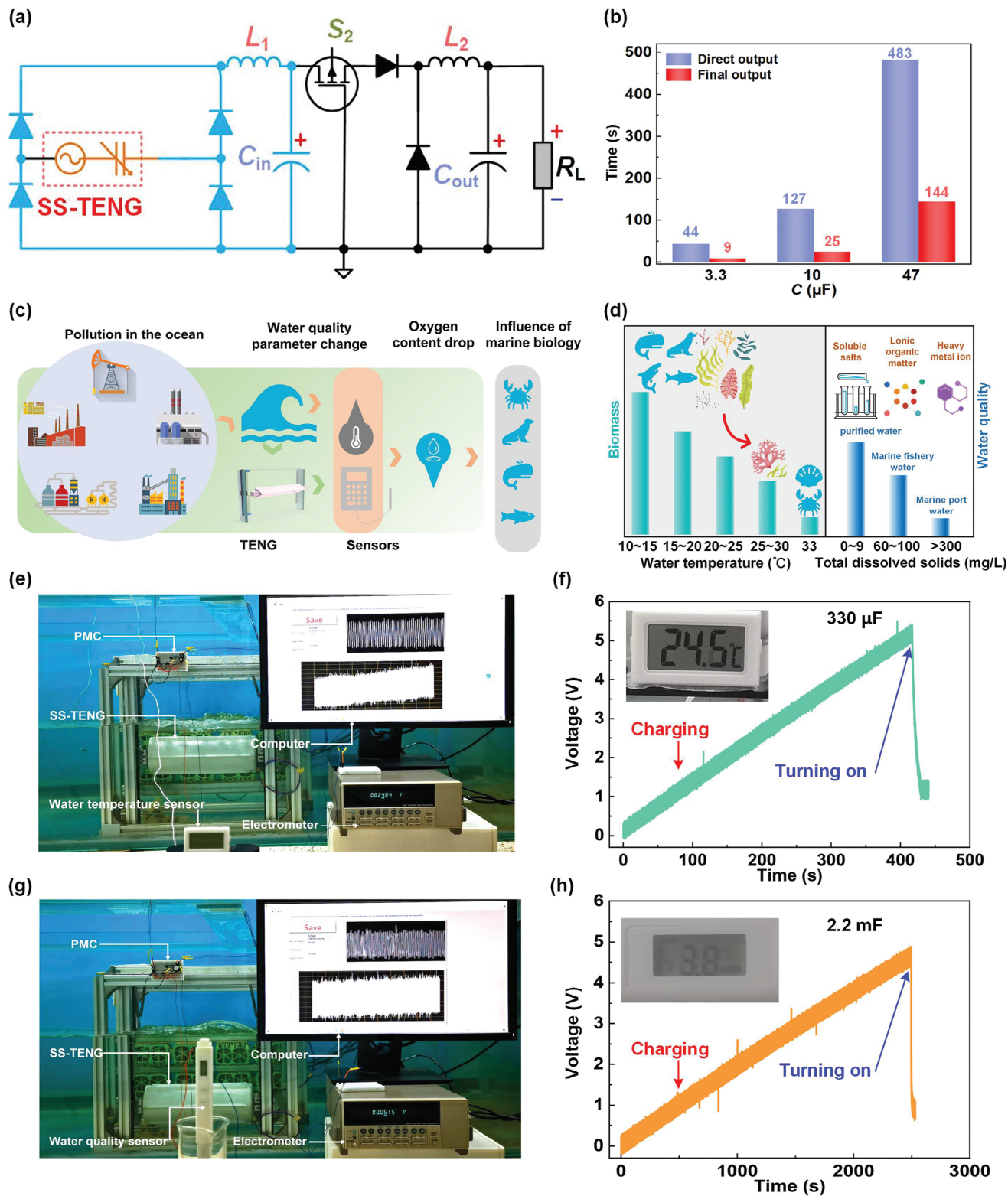


Figure 6. The SS-TENG application experiment. a) Capacitor charging circuit. b) Comparison of capacitor charging time with and without circuit. c) Purpose of water pollution monitoring. d) Principle of water pollution monitoring by temperature and quality. e) Water temperature monitoring system. f) Water temperature sensor working process. g) Water quality monitoring system. h) Water quality sensor operation.

capacitor (C_{out}) and supplied to the load. The detailed process is shown in Figure S10 (Supporting Information). As demonstrated by charging experiments with three different capacitors charged to 3.3 V, the charging speed using the PMC is obviously faster than direct output (Figure 6b), showing a marked improvement in charging efficiency.

Tidal current energy is primarily concentrated near coastal areas, where rapid industrialization and urbanization have led to the direct or indirect discharge of pollutants, resulting in a continuous increase in pollutant concentration (Figure 6c). This significantly impacts biodiversity in coastal waters (Figure 6d), creating an urgent need for new self-powered monitoring systems. Figure 6e presents a thermal pollution detection system based on the SS-TENG, which utilizes seawater temperature data to monitor marine thermal pollution. In this system, the storage capacitor (330 μF) charges to 5.5 V within 6 minutes (Figure 6f), providing power to the temperature sensor for water temperature monitoring (Movie S3, Supporting Information). For a self-powered total dissolved solids (TDS) sensor, as shown in Figure 6g,h, the SS-TENG charges a 2.2 mF capacitor to 5 V within 43 minutes, enabling the detection of solid waste pollution (Movie S4, Supporting Information). Due to the scalability of the SS-TENG, it can be developed into large-scale networks for efficient tidal energy harvesting in coastal regions, as well as integrated into marine pollution monitoring systems to track pollutant levels and their diffusion trajectories.

3. Conclusion

This study presents a switch-shuttling triboelectric nanogenerator (SS-TENG), which significantly enhances the performance of traditional triboelectric nanogenerators by improving Q_{SC} , V_{OC} , and I_{SC} while also reducing internal resistance. Theoretical analysis indicates that the SS-TENG, coordinated by a synchronous switch, maintains a constant charge while the TENG capacitance decreases, thereby increasing the potential difference between the plates. This mechanism optimizes charge leakage during operation and enhances output efficiency. Experimental results indicate that the performance of the SS-TENG is significantly enhanced compared to the traditional CS-TENG, with a charge transfer capability increase of approximately 1.9 times and an I_{SC} improvement of about 9.6 times. Furthermore, the internal resistance of the SS-TENG has been reduced from 200 M Ω to only 10 M Ω , and the per-wave energy (7.28 μJ) output of the SS-TENG is 6.11 times greater than that of the CS-TENG, showcasing its practical advantages without the necessity for auxiliary circuit components or extensive processing of the triboelectric materials. The scalability of the SS-TENG for environmental applications is emphasized, as it is capable of harvesting both wave energy (with an I_{SC} of 51.3 μA and a Q_{SC} of 276.0 nC) and flow energy (with a peak power of 3.11 mW) based on the novel CHB design, making it particularly suitable for tidal current energy environments. This dual capability enables effective monitoring of marine pollution by powering sensors in areas near coastlines. The findings underscore the potential of SS-TENG technology as a foundational component for energy harvesting networks, advancing the development of renewable energy applications and environmental sustainability.

4. Experimental Section

Fabrication of the Prototype: The prototype consists of a bluff body, an internal waterproof shell, and a single-degree-of-freedom SS-TENG. The bluff body was manufactured using 3D printing technology with polylactic acid (PLA) as the material. The guide rails and sliders were made from aluminum alloy through cutting processes, while the spring was fabricated from stainless steel, with a wire diameter of 0.5 mm, an outer diameter of 10 mm, and a length of 100 mm. The internal waterproof shell of the bluff body was made from acrylic in the shape of a cylindrical tube. The SS-TENG unit was integrated within the cavity of the bluff body. The TENG unit utilizes nylon (25 μm thickness) and FEP (30 μm thickness) as the electrode materials, which were adhered to a copper surface (50 μm thickness), with acrylic serving as the substrate. The size of each electrode was 160 mm \times 70 mm.

Measuring Instrument: The vertical contact-separation process of the SS-TENG was performed using a LinMot linear motor (B01-37 \times 166/360). The various water flow velocities in the laboratory were generated by six water pumps (AQ12000DP, Huitian, China), and the detailed speed was measured by a current meter (LS300-A, Zhuoma, China). Voltage, current, and charge measurements were conducted using an electrometer (Keithley 6514). For current measurements exceeding the range of the 6514, a Tektronix mixed-domain oscilloscope (MDO34) along with a current probe (TCP312A/TCPA300) was used.

Supporting Information

Supporting Information is available from the Wiley Online Library or from the author.

Acknowledgements

X.G, Y.W, and Y.F. contributed equally to this work. This work was supported by the Beijing Natural Science Foundation (No. L244004), the Beijing Natural Science Foundation (No. 3244038), the China Postdoctoral Science Foundation (No. 2024M753185), and the National Key R & D Project from the Minister of Science and Technology (No. 2021YFA1201604).

Conflict of Interest

The authors declare no conflict of interest.

Data Availability Statement

The data that support the findings of this study are available from the corresponding author upon request. Source data are provided with this paper.

Keywords

dual-energy harvesting, enhanced output performance, marine pollution, reduced internal resistance, triboelectric nanogenerator

Received: November 2, 2024
Revised: December 9, 2024
Published online: December 23, 2024

- [1] D. Butler, *Nature* **2006**, 440, 402.
- [2] E. Borgia, *Comput. Commun.* **2014**, 54, 1.
- [3] E. J. Markvicka, M. D. Bartlett, X. Huang, C. Majidi, *Nat. Mater.* **2018**, 17, 618.

- [4] Z. Zhao, L. Zhou, S. Li, D. Liu, Y. Li, Y. Gao, Y. Liu, Y. Dai, J. Wang, Z. L. Wang, *Nat. Commun.* **2021**, *12*, 4686.
- [5] Z. L. Wang, *Mater. Today* **2017**, *20*, 74.
- [6] Z. Zhao, Y. Dai, D. Liu, L. Zhou, S. Li, Z. L. Wang, J. Wang, *Nat. Commun.* **2020**, *11*, 6186.
- [7] W. Yan, Y. Liu, P. Chen, L. N. Y. Cao, J. An, T. Jiang, W. Tang, B. Chen, Z. L. Wang, *Adv. Energy Mater.* **2022**, *12*, 2103677.
- [8] G. Gu, G. Gu, W. Shang, Z. Zhang, W. Zhang, C. Wang, D. Fang, G. Cheng, Z. Du, *Nano Energy* **2022**, *102*, 107699.
- [9] F.-R. Fan, Z.-Q. Tian, Z. L. Wang, *Nano Energy* **2012**, *1*, 328.
- [10] D. Zhu, X. Guo, H. Li, Z. Yuan, X. Zhang, T. Cheng, *Nano Energy* **2023**, *108*, 108233.
- [11] S. He, Z. Wang, X. Zhang, Z. Yuan, Y. Sun, T. Cheng, Z. L. Wang, *ACS Appl. Mater. Interfaces* **2022**, *14*, 2825.
- [12] W. Ma, P. Wang, B. Zhang, X. Li, Y. Gao, Z. Zhao, D. Liu, C. Li, J. Wang, *Adv. Energy Mater.* **2024**, *14*, 2304331.
- [13] W. Zhang, G. Gu, Z. Zhang, H. Ren, H. Zhou, Y. Gui, Z. Du, G. Cheng, *Nano Energy* **2024**, *127*, 109987.
- [14] Z. Zhang, G. Gu, W. Zhang, G. Gu, W. Shang, Y. Liu, G. Cheng, Z. Du, *Nano Energy* **2023**, *110*, 108360.
- [15] Q. Wang, D. Hu, X. Huang, Z. Chen, Z. Yuan, L. Zhong, Q. Sun, F. Wang, S. Xu, S. Chen, *Adv. Energy Mater.* **2024**, <https://doi.org/10.1002/aenm.202403931>.
- [16] Y. Yang, L. Zheng, J. Wen, F. Xing, H. Liu, Y. Shang, Z. L. Wang, B. Chen, *Adv. Funct. Mater.* **2023**, *33*, 2304366.
- [17] H. Zhang, G. Dai, Y. Luo, T. Zheng, T. Xionsong, K. Yin, J. Yang, *ACS Energy Lett.* **2024**, *9*, 1431.
- [18] K. Li, C. Shan, S. Fu, H. Wu, W. He, J. Wang, G. Li, Q. Mu, S. Du, Q. Zhao, C. Hu, *Energy Environ. Sci.* **2024**, *17*, 580.
- [19] Z. Zhang, G. Gu, W. Zhang, Z. Du, G. Cheng, *Nano Energy* **2024**, *131*, 110308.
- [20] T. Wang, C. Wang, Q. Zeng, G. Gu, X. Wang, G. Cheng, Z. Du, *Nano Energy* **2024**, *125*, 109533.
- [21] S. Wu, J. Yang, Y. Wang, B. Liu, Y. Xiong, H. Jiao, Y. Liu, R. Bao, Z. L. Wang, Q. Sun, *Adv. Sustain. Syst.* **2023**, *7*, 2300135.
- [22] L. Xu, T. Jiang, P. Lin, J. J. Shao, C. He, W. Zhong, X. Y. Chen, Z. L. Wang, *ACS Nano* **2018**, *12*, 1849.
- [23] C. Zhang, W. Yuan, B. Zhang, J. Yang, Y. Hu, L. He, X. Zhao, X. Li, Z. L. Wang, J. Wang, *Small* **2023**, *19*, 2304412.
- [24] X. Wang, Q. Gao, M. Zhu, J. Wang, J. Zhu, H. Zhao, Z. L. Wang, T. Cheng, *Appl. Energy* **2022**, *323*, 119648.
- [25] Q. Wang, D. Hu, X. Huang, Z. Yuan, L. Zhong, Q. Sun, F. Wang, S. Xu, S. Chen, *Adv. Funct. Mater.* **2024**, *34*, 2409088.
- [26] S. Xu, J. Wang, H. Wu, Q. Zhao, G. Li, S. Fu, C. Shan, K. Li, Z. Zhang, C. Hu, *Adv. Mater.* **2024**, *36*, 2312148.
- [27] J. Wang, S. Xu, G. Li, X. Zhang, Q. Zhao, H. Wu, K. Li, S. Fu, C. Shan, W. He, C. Hu, *Adv. Energy Mater.* **2024**, *14*, 2400429.
- [28] G. Cheng, Z. Lin, L. Lin, Z. Du, Z. L. Wang, *ACS Nano* **2013**, *7*, 7383.
- [29] Q. Zhao, H. Wu, J. Wang, S. Xu, W. He, C. Shan, S. Fu, G. Li, K. Li, C. Hu, *Adv. Energy Mater.* **2023**, *13*, 2302099.
- [30] S. Wang, Y. Xie, S. Niu, L. Lin, C. Liu, Y. S. Zhou, Z. L. Wang, *Adv. Mater.* **2014**, *26*, 6720.
- [31] L. Liu, L. Zhou, C. Zhang, Z. Z., S. L., X. Li, X. Yin, J. Wang, Z. L. Wang, *J. Mater. Chem. A* **2021**, *9*, 21357.
- [32] Z. Zhao, L. Zhou, S. Li, D. Liu, Y. Li, Y. Gao, Y. Liu, Y. Dai, J. Wang, Z. L. Wang, *Nat. Commun.* **2021**, *12*, 4686.
- [33] G. Liu, H. Guo, S. Xu, C. Hu, Z. L. Wang, *Adv. Energy Mater.* **2019**, *9*, 1900801.
- [34] Y. Yu, Q. Gao, X. Zhang, D. Zhao, X. Xia, J. Wang, H. Li, Z. L. Wang, T. Cheng, *Energy Environ. Sci.* **2023**, *16*, 3932.
- [35] Y. Yu, H. Li, X. Zhang, Q. Gao, B. Yang, Z. L. Wang, T. Cheng, *Joule* **2024**, *8*, 1855.
- [36] X. Chen, Y. Zhao, F. Wang, D. Tong, L. Gao, D. Li, L. Wu, X. Mu, Y. Yang, *Adv. Sci.* **2022**, *9*, 2103957.
- [37] F.-R. Fan, L. Lin, G. Zhu, W. Wu, R. Zhang, Z. L. Wang, *Nano Lett.* **2012**, *12*, 3109.
- [38] S. Li, J. Nie, Y. Shi, X. Tao, F. Wang, J. Tian, S. Lin, X. Chen, Z. L. Wang, *Adv. Mater.* **2020**, *32*, 2001307.
- [39] H. Wang, L. Xu, Y. Bai, Z. L. Wang, *Nat. Commun.* **2020**, *11*, 4203.
- [40] Z. Yang, Y. Yang, H. Wang, F. Liu, Y. Lu, L. Ji, Z. L. Wang, J. Cheng, *Adv. Energy Mater.* **2021**, *11*, 2101147.
- [41] L. Xu, T. Bu, X. Yang, C. Zhang, Z. L. Wang, *Nano Energy* **2018**, *49*, 625.
- [42] W. Liu, Z. Wang, G. Wang, G. Liu, J. Chen, X. Pu, Y. Xi, X. Wang, H. Guo, C. Hu, Z. L. Wang, *Nat. Commun.* **2019**, *10*, 1426.
- [43] J. Zhang, Y. Gao, D. Liu, J. Zhao, J. Wang, *Nat. Commun.* **2023**, *14*, 3218.
- [44] Y. Xia, J. Zhi, R. Zhang, F. Zhou, S. Liu, Q. Xu, Y. Qin, *Adv. Mater.* **2024**, *36*, 2403361.
- [45] P. Vasandani, B. Gattu, Z. Mao, W. Jia, M. Sun, *Nano Energy* **2018**, *43*, 210.